The Astrophysical Journal, 582:1206–1219, 2003 January 10

THE DYNAMIC EVOLUTION OF TWISTED MAGNETIC FLUX TUBES IN A THREE-DIMENSIONAL CONVECTING FLOW. I. UNIFORMLY BUOYANT HORIZONTAL TUBES

Y. Fan
High Altitude Observatory, National Center for Atmospheric Research,[1] 3450 Mitchell Lane, Boulder, CO 80301;
and Institute for Theoretical Physics, University of California, Santa Barbara, CA 93106

and

W. P. Abbett and G. H. Fisher
Space Sciences Laboratory, University of California, Berkeley, CA 94720; and Institute for Theoretical Physics,
University of California, Santa Barbara, CA 93106
Received 2002 July 4; accepted 2002 September 19

ABSTRACT

We present three-dimensional numerical simulations of the dynamic evolution of uniformly buoyant, twisted horizontal magnetic flux tubes in a three-dimensional stratified convective velocity field. Our calculations are relevant to understanding how stratified convection in the deep solar convection zone may affect the rise and the structure of buoyant flux tubes that are responsible for the emergence of solar active regions. We find that in order for the magnetic buoyancy force of the tube to dominate the hydrodynamic force due to the convective downflows, the field strength B of the flux tube needs to be greater than $(H_p/a)^{1/2}B_{\rm eq} \sim 3B_{\rm eq}$, where H_p is the pressure scale height, a is the tube radius, and $B_{\rm eq}$ is the field strength in equipartition with the kinetic energy density of the strong downdrafts. For tubes of equipartition field strength ($B = B_{\rm eq}$), the dynamic evolution depends sensitively on the local condition of the convective flow. Sections of the tube in the paths of strong downdrafts are pinned down to the bottom despite their buoyancy, while the rise speed of sections within upflow regions is significantly boosted; Ω-shaped emerging tubes can form between downdrafts. Although flux tubes with $B = B_{\rm eq}$ are found to be severely distorted by convection, the degree of distortion obtained from our simulations is not severe enough to clearly rule out the Ω-tubes that are able to emerge between downdrafts as possible progenitors of solar active regions. As the initial field strength of the tube becomes higher than the critical value of $\sim(H_p/a)^{1/2}B_{\rm eq}$ given above, the dynamic evolution converges toward the results of previous simulations of the buoyant rise of magnetic flux tubes in a static, adiabatically stratified model solar convection zone. Tubes with 10 times the equipartition field strength are found to rise unimpeded by the downdrafts and are not significantly distorted by the three-dimensional convective flow.

Subject headings: convection — methods: numerical — MHD — Sun: interior — Sun: magnetic fields

1. INTRODUCTION

If the magnetic field seen in sunspots and active regions on the solar surface originates from a strong toroidal magnetic field generated by the dynamo mechanism at the base of the solar convection zone, then the question of how magnetic flux is transported through the convection zone must be addressed. Many existing models posit that magnetic flux rises buoyantly through the convection zone in the form of discrete flux tubes and that the tubes must maintain reasonable cohesion in order for the emerging flux to be organized as active regions, which display a well-defined order, as described by Hale's polarity rule and Joy's law of active region tilts (Hale et al. 1919; Howard 1991; Fisher, Fan, & Howard 1995). Many dynamic calculations of the subsurface evolution of buoyant magnetic flux tubes in the solar convection zone have been carried out. One method that has been widely used is the "thin flux tube formulation" (Spruit 1981), in which the flux tube is treated as a one-dimensional curve moving in the space of a model solar convective envelope, acted on by magnetic buoyancy, tension, aerodynamic drag, and the Coriolis force. Calculations based on the thin flux tube model find that the field strength of toroidal flux tubes at the base of the solar convection zone needs to be substantially superequipartition compared to the kinetic energy density of convection (with B ranging from 3×10^4 to 10^5 G) in order for the emerging tubes to be consistent with the observed properties of solar active regions (see, e.g., the reviews by Moreno-Insertis 1997; Fisher et al. 2000).

Recently, more sophisticated multidimensional MHD simulations of the subsurface evolution of rising magnetic flux tubes have been carried out that address important issues of the dynamics that cannot be addressed within the thin flux tube framework: issues such as the cohesion of the rising flux tubes and the effects of field line twist. Two-dimensional simulations of the buoyant rise of twisted, horizontal flux tubes have shown that a minimum amount of twist is needed for the flux tube to rise cohesively (e.g., Longcope, Fisher, & Arendt 1996; Dorch & Nordlund 1998; Emonet & Moreno-Insertis 1998; Fan, Zweibel, & Lantz 1998). In two dimensions, an untwisted horizontal tube splits into a pair of counterrotating vortex tubes that move apart horizontally and cease to rise. Three-dimensional simulations of arched, Ω-shaped flux tubes show that the amount of twist needed for a cohesive rise of the flux tube may be substantially reduced in comparison to the two-dimensional case (Wissink et al. 2000; Abbett, Fisher, & Fan 2000, 2001; Fan 2001).

[1] The National Center for Atmospheric Research is sponsored by the National Science Foundation.

Most multidimensional simulations (e.g., all of the ones cited above) have modeled the rise of the flux tubes in a static, adiabatically stratified model solar convection without explicitly including convective velocity fields. The basic argument to justify such a treatment is that if the magnetic field strength of the flux tube is sufficiently superequipartition in comparison to the kinetic energy of the convective flow, the distortion of the flux tube due to convection would be small, and its dynamic influence on the rising flux tube can be ignored. The above qualitative argument is yet to be tested and quantified by explicit calculations. Recently, Dorch et al. (2001) performed the first three-dimensional MHD simulations of a buoyant magnetic flux rope in a stratified convecting model convection zone. They focused on one particular case in which the tube is initially located in an upflow region and its field strength is adequately superequipartition such that the tube retains its initial shape during its ascent. In this paper, we present a set of numerical simulations of the dynamic evolution of buoyant magnetic flux tubes in a three-dimensional stratified convective velocity field, exploring an extensive range of parameter space. We consider buoyant tubes with field strengths that range from $B_{\rm eq}$ to $10B_{\rm eq}$, where $B_{\rm eq}$ is the field strength in equipartition with the kinetic energy density of the strong convective downdrafts. We also vary the twist of the tube from 0 to an amount that is just above the critical value required for tube cohesion as determined from previous two-dimensional calculations (Emonet & Moreno-Insertis 1998; Fan et al. 1998). To clearly isolate the effect of convection, we consider in this paper only tubes with a uniform distribution of buoyancy along the initial tube such that in the absence of convection, the tubes remain horizontal, corresponding to previous two-dimensional simulations of the rise of twisted horizontal flux tubes (e.g., Emonet & Moreno-Insertis 1998; Fan et al. 1998). Any development of three-dimensionality in the tube structure in the subsequent evolution is caused by the three-dimensional convective flow. We investigate under what conditions and to what extent results from previous calculations of rising flux tubes in the absence of convection remain valid.

The organization of this paper is as follows. In § 2 we describe the anelastic numerical model and the setup of the simulations. The simulation results are presented in § 3, and the conclusions are summarized and discussed in § 4.

2. THE NUMERICAL MODEL

We use the anelastic approximation of the MHD equations to model the interaction between buoyant magnetic flux tubes and convection deep in the solar convection zone. The anelastic approximation is suitable for numerical simulations of subsonic, dynamic processes in the high-β plasma of the solar (or stellar) interior. The detailed derivation of the anelastic MHD equations has been described elsewhere (see, e.g., Gilman & Glatzmaier 1981; Glatzmaier 1984; Lantz & Fan 1999). Here we directly list the anelastic equations, which we solve numerically:

$$\nabla \cdot (\rho_0 \boldsymbol{v}) = 0 \,, \tag{1}$$

$$\rho_0 \left[\frac{\partial \boldsymbol{v}}{\partial t} + (\boldsymbol{v} \cdot \nabla)\boldsymbol{v} \right] = -\nabla p_1 + \rho_1 \boldsymbol{g} + \frac{1}{4\pi} (\nabla \times \boldsymbol{B}) \times \boldsymbol{B} + \nabla \cdot \boldsymbol{\Pi} \,, \tag{2}$$

$$\rho_0 T_0 \left[\frac{\partial s_1}{\partial t} + (\boldsymbol{v} \cdot \nabla)(s_0 + s_1) \right] = \nabla \cdot (K \rho_0 T_0 \nabla s_1) + \frac{1}{4\pi} \eta |\nabla \times \boldsymbol{B}|^2 + (\boldsymbol{\Pi} \cdot \nabla) \cdot \boldsymbol{v} \,, \tag{3}$$

$$\nabla \cdot \boldsymbol{B} = 0 \,, \tag{4}$$

$$\frac{\partial \boldsymbol{B}}{\partial t} = \nabla \times (\boldsymbol{v} \times \boldsymbol{B}) - \nabla \times (\eta \nabla \times \boldsymbol{B}) \,, \tag{5}$$

$$\frac{\rho_1}{\rho_0} = \frac{p_1}{p_0} - \frac{T_1}{T_0} \,, \tag{6}$$

$$\frac{s_1}{c_p} = \frac{T_1}{T_0} - \frac{\gamma - 1}{\gamma} \frac{p_1}{p_0} \,. \tag{7}$$

In the above, ρ_0, $p_0(z)$, $T_0(z)$, and $s_0(z)$ denote a time-independent, plane-parallel reference atmosphere that is assumed to be in hydrostatic equilibrium and *nearly* adiabatically stratified, and the equations solve for the evolution of the velocity $\boldsymbol{v}$, magnetic field $\boldsymbol{B}$, and the thermodynamic fluctuations s_1, p_1, ρ_1, and T_1, which represent perturbations from the reference state. The quantity $\boldsymbol{g}$ denotes the gravitational acceleration, which is assumed constant. The quantity $\boldsymbol{\Pi}$ is the viscous stress tensor,

$$\Pi_{ij} \equiv \rho_0 \nu \left[\frac{\partial v_i}{\partial x_j} + \frac{\partial v_j}{\partial x_i} - \frac{2}{3} (\nabla \cdot \boldsymbol{v}) \delta_{ij} \right] \,, \tag{8}$$

and ν, K, and η denote the kinematic viscosity, thermal diffusivity, and magnetic diffusivity, respectively. We assume that ν, K, and η are constant throughout the simulation domain.

We assume for the reference atmosphere a *weakly* superadiabatically stratified polytrope:

$$\rho_0(z) = \rho_r \left[1 - \frac{z}{(m+1)H_r} \right]^m \,, \tag{9}$$

$$p_0(z) = p_r \left[1 - \frac{z}{(m+1)H_r} \right]^{m+1} \,, \tag{10}$$

$$T_0(z) = T_r \left[1 - \frac{z}{(m+1)H_r} \right] \,, \tag{11}$$

$$\frac{ds_0}{dz} = -\frac{c_p \delta(z)}{H_p} \,, \tag{12}$$

$$\delta(z) = \delta_r \frac{\rho_r}{\rho_0(z)} \,, \tag{13}$$

where T_r, ρ_r, p_r, and H_r are respectively the values of T_0, ρ_0, p_0, and H_p (the pressure scale height) at $z = 0$, c_p is the specific heat at constant pressure, and m is the polytropic index. In the above, $\delta(z)$ is the nondimensional superadiabaticity, whose magnitude is assumed to be $\ll 1$. The quantity δ_r denotes the value of δ at $z = 0$. Since $|\delta| \ll 1$, the value m is essentially unchanged from the adiabatic value: $m = 1/(\gamma - 1)$, where γ is the ratio of specific heats and

where for an ideal gas $\gamma = 5/3$. The reference state profile $s_0(z)$ given by equations (12) and (13) is a steady state solution of the thermal diffusion equation $\nabla \cdot (K\rho_0 T_0 \nabla s_0) = 0$, assuming constant K. The equilibrium reference atmosphere is convectively unstable because of the negative gradient in s_0.

We want to note that unlike the other thermodynamic quantities with subscript "0" (e.g., T_0, p_0, and ρ_0), here s_0 is a first-order $O(\delta)$ quantity (compared to the zero-order quantity c_p) in the anelastic scaling. Through equation (12), a small first-order entropy gradient ds_0/dz with a magnitude $\sim\delta(c_p/H_p) \ll c_p/H_p$ is introduced into the reference state to make the reference atmosphere convectively unstable (see also Glatzmaier 1984, p. 464). As convection develops, the entropy field in the domain is subsequently adjusted by the time-dependent s_1, which is also an $O(\delta)$ quantity. Therefore, s_0 and s_1 are both $O(\delta)$, and it is *not* assumed that s_1 is small compared to s_0. In fact, the final entropy gradient $d\bar{s}(z)/dz = ds_0(z)/dz + d\bar{s}_1(z)/dz$, obtained when the convection reaches a statistical equilibrium, may be significantly different from the reference state $ds_0(z)/dz$. (In the above, the overbar indicates horizontal average.) The anelastic approximation remains valid as long as the total entropy gradient $d\bar{s}(z)/dz$ remains small compared to c_p/H_p, or in other words, if we assume that the entropy value is 0 at the bottom of the domain, then the magnitude of the entropy $s = s_0 + s_1$ in the domain should remain small compared to c_p. These requirements remain satisfied throughout our simulations (see discussion about Fig. 2 below). We also note that there is a difference in the definition of the reference atmosphere used in the present paper compared to that in Lantz & Fan (1999), which we describe in the Appendix.

We solve the three-dimensional anelastic MHD equations in a rectangular Cartesian domain with periodic boundary conditions in the horizontal directions and nonpenetrating, stress-free upper and lower boundaries. We also assume that the bottom boundary is an infinitely conducting plate for the magnetic field and that at the top boundary the magnetic field connects smoothly to a potential field. The vertical (z) size of the domain is $L = 2.18H_r$, which spans 3 density scale heights. The ratio of the density between the top ($z = L$) and the bottom ($z = 0$) is 0.05. The two horizontal dimensions (x and y) of the simulation domain are set to the same size $4L = 8.72H_r$. Thus, the undulatory Parker instability is not playing a role here, since the domain size is below the minimum wavelength (about $11H_r$; see, e.g., Spruit & van Ballegooijen 1982) required for the onset of the instability. At the top and bottom boundaries, the entropy change s_1 is set to 0 so that the values of entropy at the top and bottom [$s_0(L)$ and $s_0(0)$] are held fixed. Therefore, a total entropy drop of $\Delta s = s_0(L) - s_0(0)$ is maintained across the simulation domain. For a fluid with nonzero viscosity and thermal diffusion, sufficient superadiabaticity is required to overcome the dissipative effect of diffusion for convection to develop, i.e., the nondimensional Rayleigh number, defined here as

$$R_a \equiv \frac{gH_r^4}{c_p K \nu}\left(\frac{\Delta s}{L}\right), \tag{14}$$

needs to exceed a critical value R_{ac}. For our simulations, $R_a = 1.3 \times 10^5$. Since our reference equilibrium atmosphere is significantly stratified, the critical Rayleigh number R_{ac} cannot be derived analytically. If we use the critical Rayleigh number of 657.5 derived under the Boussinesq approximation (Rayleigh 1916; Chandrasekhar 1961) as an estimate of R_{ac} for our equilibrium atmosphere, we have $R_a \sim 200R_{ac}$. We also used direct anelastic simulations of the growth of initial random perturbations under different Rayleigh numbers to roughly estimate what the critical R_{ac} is. From this estimate, we obtain $R_a \sim 300R_{ac}$. The above estimates show that the fluid with $R_a = 1.3 \times 10^5$ is amply supercritical for the onset of convection. The magnitude of the diffusive parameters ν, K, and η can be expressed in terms of the following nondimensional numbers: the Reynolds number $\mathrm{Re} \equiv v_c H_r/\nu$, the Prandtl number $\mathrm{Pr} \equiv \nu/K$, and the magnetic Reynolds number $\mathrm{Re}_m \equiv v_c H_r/\eta$, where the velocity scale $v_c \equiv (8\delta_r g H_r)^{1/2}$. Throughout the remainder of the paper, velocity is expressed in units of v_c. The values of the above nondimensional numbers for our simulations are given in Table 1. The details of the numerical algorithm used to solve the set of anelastic equations is described in the Appendix of Fan et al. (1999). Briefly, we use a mixed pseudospectral and finite-difference formulation, where the governing equations are

TABLE 1
PARAMETERS FOR THE SIMULATIONS

Label[a]	Grid[b]	$B_0/B_{\rm eq}$	qa	a/H_r	$\mathrm{Re} \equiv v_c H_r/\nu$	$\mathrm{Re}_m \equiv v_c H_r/\eta$	$\mathrm{Pr} \equiv \nu/K$
Conv.....	$384 \times 384 \times 96$	0	N/A	N/A	260	N/A	1
Case A	$384 \times 384 \times 96$	1	0.25	0.136	260	5000	1
Case B.....	$384 \times 384 \times 96$	3	0.25	0.136	260	1667	1
Case C.....	$384 \times 384 \times 96$	5	0.25	0.136	260	1000	1
Case D	$384 \times 384 \times 96$	10	0.25	0.136	260	500	1
Case E.....	$384 \times 384 \times 96$	1	0	0.136	260	5000	1
Case F.....	$384 \times 384 \times 96$	10	0	0.136	260	500	1
Ref A	$2 \times 384 \times 96$	1	0.25	0.136	260	5000	1
Ref D	$2 \times 384 \times 96$	10	0.25	0.136	260	500	1
Ref E.....	$2 \times 384 \times 96$	1	0	0.136	260	5000	1
Ref F.....	$2 \times 384 \times 96$	10	0	0.136	260	500	1

[a] The run marked "Conv" is the initial field-free convection simulation that evolves the convective flow to a statistical equilibrium for use in subsequent simulations of rising flux tubes. The runs marked with "Ref" are reference simulations of rising flux tubes in a static, adiabatically stratified fluid.

[b] Values are (x, y, z).

Fourier decomposed in the two horizontal directions and the vertical derivatives are written in a centered, fourth-order finite-difference form. The equations are then time-advanced using a semi-implicit method for which a second-order Adams-Bashforth scheme is used for the nonlinear advection terms and a second-order Crank-Nicholson scheme is applied to the diffusion terms.

We initiate convection with a small, random s_1 field and numerically solve the anelastic equations (with $\boldsymbol{B} = 0$) until the convective velocity field reaches a statistical steady state. (This simulation is labeled as "Conv" in Table 1.) From equations (2), (3), and (5), and the boundary conditions described earlier, a global energy conservation law can be derived (e.g., Glatzmaier 1984):

$$\frac{\partial}{\partial t}\int_V \left(\frac{1}{2}\rho_0 v^2 + \frac{B^2}{8\pi} + \rho_0 T_0 s_1\right) dV = \int_S \left(K\rho_0 T_0 \nabla s_1 - \frac{1}{4\pi}\boldsymbol{E}\times\boldsymbol{B}\right)\cdot d\boldsymbol{S}\,. \quad (15)$$

In the absence of a magnetic field, equation (15) shows that the change of the total perturbation energy in the domain, which consists of the sum of the kinetic energy $E_k \equiv \int_V \frac{1}{2}\rho_0 v^2\, dV$ and the perturbation thermal energy $E_{\rm th} \equiv \int_V \rho_0 T_0 s_1\, dV$, is determined by the diffusive heat flux $F_{\rm diff} = \int_S (K\rho_0 T_0 \nabla s_1)\cdot d\boldsymbol{S}$ through the top and bottom boundary surfaces. Figure 1 shows the variation of E_k, $E_{\rm th}$, $E_{\rm tot} \equiv E_k + E_{\rm th}$, and $F_{\rm diff}$ at the top and the bottom boundaries and the maximum velocity $v_{\rm max}$ in the simulation domain, over a period of about $122H_r/v_c$ after the convection has relaxed to a statistical steady state. It can be seen that the energies in the domain have reached steady values with the diffusive heat fluxes through the top and bottom being nearly equal, indicating that the global energy conservation is well satisfied by our numerical code. (Note that the code is not written in the energy-conservative form.) The maximum velocity in the simulation domain is about $1.25v_c$.

The top panel of Figure 2 shows the steady state vertical profile of the mean specific entropy $\overline{s}(z) = s_0(z) + \overline{s}_1(z)$ in the convecting box. The overbar indicates the horizontal average. The dashed line shows the initial entropy profile $s_0(z)$ for comparison. As described earlier, the boundary values of entropy at the top $[\overline{s}(L) = s_0(L)]$ and bottom $[\overline{s}(0) = s_0(0)]$ are held fixed, and hence the convection in our calculation is driven by a fixed entropy drop across the simulation domain. The final steady state profile $\overline{s}(z)$ is nearly flat (isentropic) throughout most of the convecting domain, with enhanced gradients near the top and the bottom boundaries compared to the initial $s_0(z)$. Such a final $\overline{s}(z)$ profile can be easily understood. In the main bulk of the domain, convection smooths out the entropy gradient and transports energy mainly in the form of advection fluxes, while at the top and bottom boundaries, the only means for carrying the energy flux through is the diffusive heat flux, which requires a gradient in entropy.

It can be seen from the top panel of Figure 2 that the magnitude of $\overline{s}(z)$ has a maximum of about $30\delta_r c_p$. Assuming that δ_r (the superadiabaticity at the bottom of the domain) is no greater than 10^{-6}, a reasonable assumption for the value of superadiabaticity near the base of the solar convection zone, then the peak magnitude of $\overline{s}(z)$ in the domain is no greater than about $3\times10^{-5}c_p$, which is much smaller than c_p, consistent with the anelastic approximation. Furthermore, the middle and the bottom panels of Figure 2 show respectively $\overline{p}_1(z)/p_0(z)$ and $\overline{T}_1(z)/T_0(z)$ in the domain, where p_1 and T_1 are the deviations from the reference state $p_0(z)$ and $T_0(z)$ and the overbar again indicates the horizontal average. It can be seen that the peak magnitudes of $\overline{p}_1(z)/p_0(z)$ and $\overline{T}_1(z)/T_0(z)$ in the domain are respectively about $70\delta_r$ and $40\delta_r$, which are no greater than 7×10^{-5} and 4×10^{-5}, given that δ_r is no greater than 10^{-6}. Therefore, $\overline{p}_1(z)/p_0(z)$ and $\overline{T}_1(z)/T_0(z)$ remain small

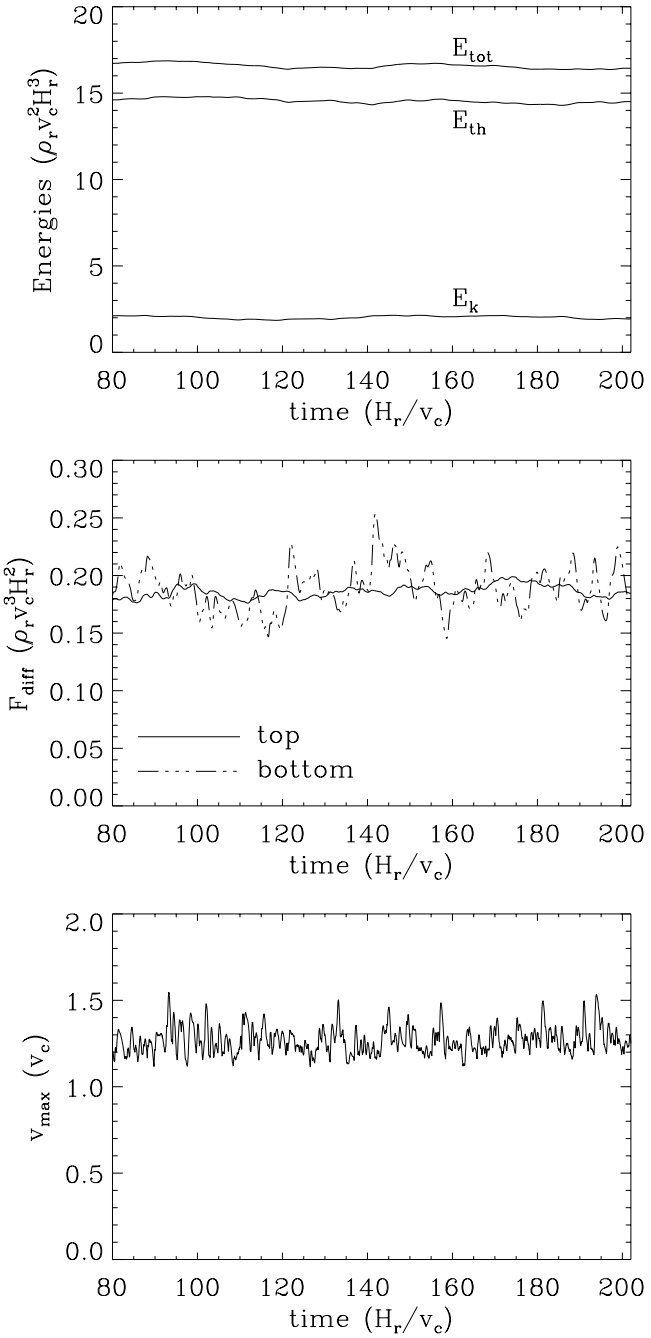

FIG. 1.—Variation with time of the kinetic energy E_k, the perturbation thermal energy $E_{\rm th}$, and the sum of the two $E_{\rm tot}$ in the simulation domain (*top*), the diffusive energy flux through the top and bottom boundaries (*middle*), and the maximum velocity in the domain (*bottom*), over a period of about $122H_r/v_c$ after the convection in the box has relaxed to a statistical steady state (from run Conv in Table 1).

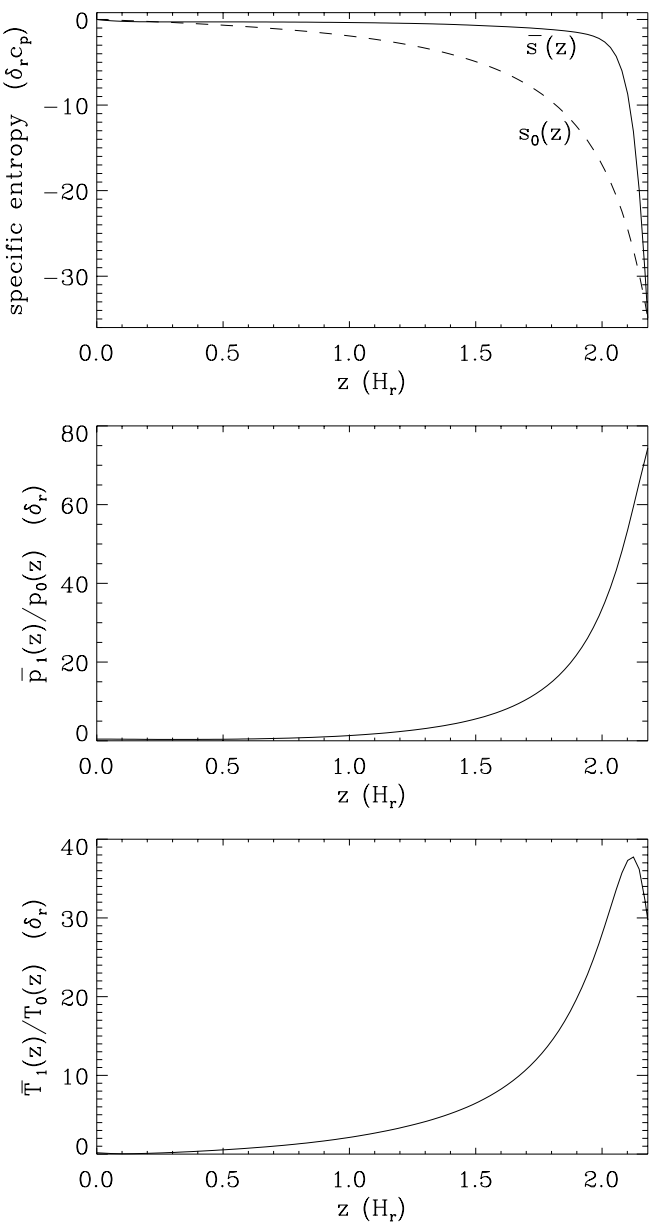

FIG. 2.—Steady state vertical profile of the mean specific entropy $\bar{s}(z) = s_0(z) + \bar{s}_1(z)$ in the convecting box after the convection has relaxed to a statistical steady state (*top*). Plots of $\bar{p}_1(z)/p_0(z)$ (*middle*) and $\bar{T}_1(z)/T_0(z)$ (*bottom*) in the domain are shown after the convection has relaxed to a statistical steady state, where p_1 and T_1 are the deviations from the reference state $p_0(z)$ and $T_0(z)$ and the overbar indicates the horizontal average (from run Conv in Table 1).

compared to 1. The anelastic approximation assumed in our calculation remains valid.

Figure 3 shows a snapshot of the vertical velocity field of the convecting box. We find that the velocity field shows the typical features of overturning convection in a stratified fluid as have been found in many previous investigations (e.g., Stein & Nordlund 1989, 2000). The surface layer displays a cellular pattern with patches of upflow region surrounded by narrow downflow lanes. In the bulk of the convecting domain, the downflows are concentrated into narrow filamentary plumes, some of which extend all the way across the domain, while the upflows are significantly broader and are of smaller velocity amplitude in comparison to the downdrafts. Figure 4 shows the maximum upflow, downflow, horizontal, and total velocities ($v_{+z\max}$, $v_{-z\max}$, $v_{x\max}$, $v_{y\max}$, $v_{\max}$) as a function of height (*top panel*) and the rms upflow, downflow, horizontal, and total velocities ($v_{+z\mathrm{rms}}$, $v_{-z\mathrm{rms}}$, $v_{x\mathrm{rms}}$, $v_{y\mathrm{rms}}$, v_{rms}) as a function of height (*bottom panel*). The asymmetry between the upflow and downflow velocities can be seen. The strongest downdrafts have a velocity comparable to v_c.

For our study of the interaction between buoyant magnetic flux tubes and stratified convection, we insert a buoyant, twisted, horizontal flux tube into the statistically steady convecting flow described above. The magnetic field of the flux tube is given by

$$\boldsymbol{B} = B_\theta(r)\hat{\boldsymbol{\theta}} + B_l(r)\hat{\boldsymbol{l}}\,, \tag{16}$$

$$B_l(r) = B_0 \exp\left(\frac{-r^2}{a^2}\right)\,, \quad B_\theta(r) = qrB_l(r)\,, \tag{17}$$

where $\hat{\boldsymbol{l}}$ denotes the tube axial direction, $\hat{\boldsymbol{\theta}}$ is the azimuthal direction in the tube cross section, and r is the radial distance to the central axis. The flux tube is uniformly twisted, and the constant q denotes the angular rate of field line rotation about the axis per unit length along the tube. The tube axis is placed at a height $z_t = 0.45H_r$, which is about one-fifth the total height of the domain. The radius of the tube is set to $a = 0.135H_r$. At the base of the solar convection zone, flux tubes responsible for emerging active regions are expected to have a radius that is on the order of or smaller than 0.1 times the local pressure scale height. This is estimated from the typical amount of flux observed in solar active regions and assuming that the tube field strength is at least in equipartition with convection. Thus, the tube size that we consider in our simulations is at the upper limit of the expected sizes of active region scale tubes at the base of the solar convection zone. We cannot model tubes of smaller sizes because of numerical constraints: our simulation domain needs to be sufficiently wide so that the convective flow is not severely constrained, but in the meantime we need to be able to adequately resolve the thin flux tube.

As we insert the flux tube into the flow, we do not alter the velocity field. In this way, the magnetized plasma of the flux tube will initially move with the original local velocity field at the time of insertion ($t = 0$) but will subsequently react to the flow via accelerations by the Lorentz force and the buoyancy force. We adjust the thermodynamic condition of the tube plasma to make it buoyant. We modify the entropy in the volume occupied by the tube by adding a change of

$$\delta s(x,\ y,\ z) = [s_0(0) - s_0(z) - s_1(x,\ y,\ z)]\exp\left(\frac{-r^2}{a^2}\right) \tag{18}$$

to the original field-free value of $s(x,\ y,\ z) = s_0(z) + s_1(x,\ y,\ z)$. As a result, the flux tube has a constant entropy along the tube axis that is equal to the value at the base of the convection zone $s_0(0)$, and the entropy of the tube merges smoothly with the external entropy field ($\delta s \to 0$) at the boundary of the tube. The flux tube is nearly uniformly buoyant along the tube, with the buoyancy force on the tube axis given by

$$f_{\mathrm{buo}} \approx \frac{B_0^2}{8\pi h_0(z_t)}\left(1 - \frac{1}{2}q^2a^2\right) + \frac{s_0(0) - s_0(z_t)}{c_p}\rho_0(z_t)g\,. \tag{19}$$

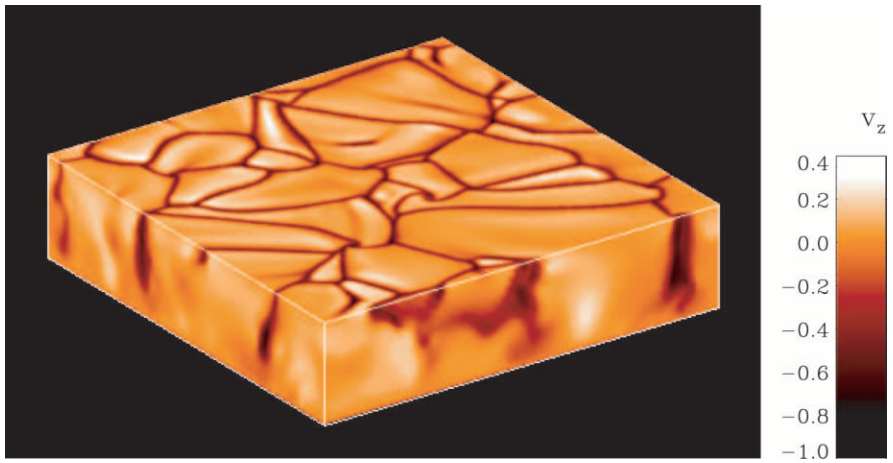

FIG. 3.—Snapshot of the vertical velocity field of the convecting box (from run Conv in Table 1)

We do a series of numerical simulations with varying axial field strength B_0 and twist q. We consider values of B_0 that range from 1 to 10, in units of the equipartition field $B_{\rm eq} \equiv (4\pi\rho_r)^{1/2} v_c$. Thus, for $B_0 = 1$, $B_0^2/8\pi = (1/2)\rho_r v_c^2$, i.e., the magnetic field is roughly in equipartition with the kinetic energy density of the strongest downdrafts. On the other hand, for $B_0 = 10$, the magnetic flux tube is highly superequipartitioned, with the magnetic energy density being about 100 times the kinetic energy density of the strongest downdrafts. A few two-dimensional reference simulations of the rise of the above buoyant horizontal flux tubes placed in a static, adiabatically stratified fluid are also done for comparison in order to better understand the effects of three-dimensional convection on the dynamic evolution of the tubes. The background fluid stratification for the reference runs is given by equations (9)–(12), with equation (12) replaced by $ds_0/dz = 0$. The parameters of all the runs are summarized in Table 1. Note that the magnetic diffusivity η or the magnetic Reynolds number Re_m is different for runs with different tube field strength B_0. This is because tubes with higher field strength require a larger magnetic diffusivity (or smaller Re_m) for numerical stability. Furthermore, the timescales for the rise differ for tubes of different field strength. When convection is ignored, the rise time of the tube scales inversely with B_0. The values of Re_m are chosen such that the ratio of the diffusive timescale (a^2/η) over the rise time is about 10 for all cases.

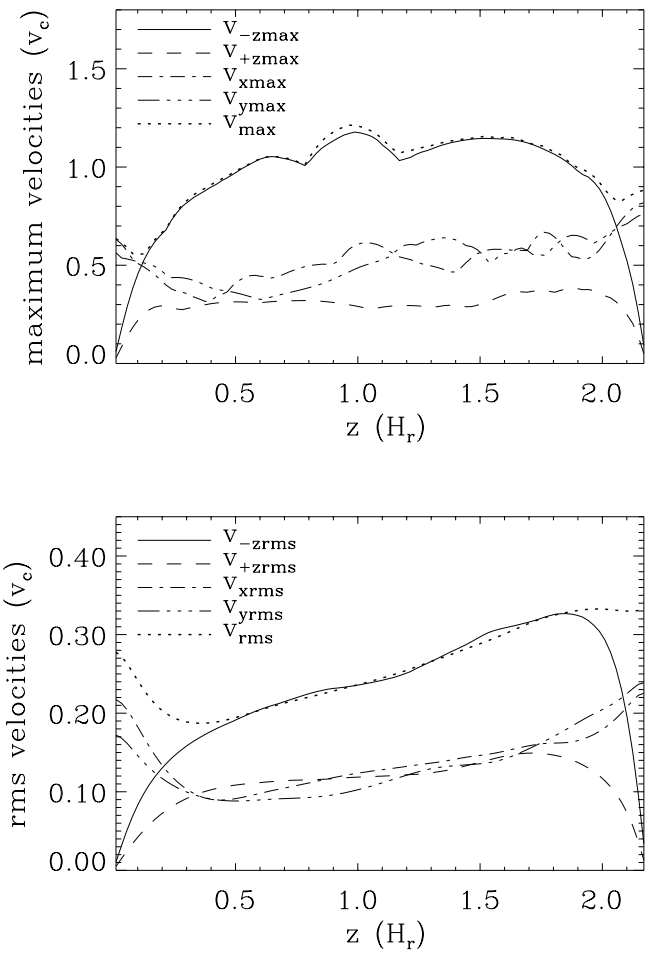

FIG. 4.—Maximum upflow, downflow, horizontal, and total velocities ($v_{+z\max}$, $v_{-z\max}$, $v_{x\max}$, $v_{y\max}$, and $v_{\max}$) as a function of height (*top*) and the rms upflow, downflow, horizontal, and total velocities ($v_{+z\mathrm{rms}}$, $v_{-z\mathrm{rms}}$, $v_{x\mathrm{rms}}$, $v_{y\mathrm{rms}}$, v_{rms}) as a function of height (*bottom*) (from run Conv in Table 1).

3. RESULTS

3.1. *Overview*

Simulation results from cases A, B, C, and D give us a clear view of how the evolution of the buoyant tubes in three-dimensional convection depends on the field strength of the tube. For these runs, the initial flux tube is inserted in the same location in the convecting box. The velocity field in the vertical slice that contains the axis of the initial flux tube at $t = 0$ is shown in Figure 5. It can be seen that there are a couple of strong downdrafts at the flux tube location. The largest velocity vector in the figure is about $0.9v_c$. The initial axial field for cases A, B, C, and D is respectively $B_0 = 1$, 3, 5, and 10 in units of $B_{\rm eq}$, and the twist is $q = 0.25a^{-1}$, being the same for all four cases (see Table 1). Previous two-dimensional simulations of the buoyant rise of horizontal flux tubes in a static convection zone found that with this amount of twist, the flux tube rises coherently through the stratified fluid (see, e.g., Emonet & Moreno-Insertis 1998; Fan et al. 1998). The subsequent evolution of the buoyant flux tube in the three-dimensional convective flow from the

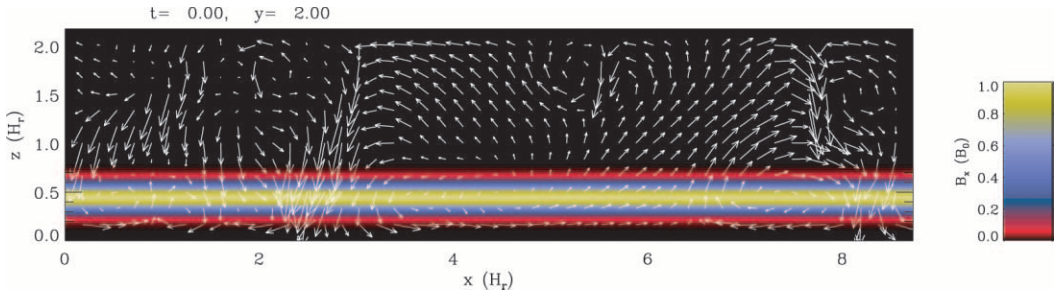

FIG. 5.—Velocity field and field B_x in the vertical plane that contains the axis of the initial tube at $t = 0$ (the same for cases A, B, C, D, E, and F in Table 1).

four runs is shown in Figure 6. The images in Figure 6 show the volume rendering of the absolute magnetic field strength of the flux tube. It can be seen that in the case with a highly superequipartition field ($B_0 = 10$; Fig. 6*d*), the rising flux tube essentially retains its initial straight horizontal configuration, except that the tube cross section deforms into a crescent shape with some small amount of weak flux being pulled behind from the edge of the tube. The evolution of the tube is essentially the same as that obtained from the reference simulation (Ref D in Table 1) with the tube placed in a static, adiabatically stratified fluid. For cases with decreasing axial field strength (Figs. 6*c*, 6*b*, and 6*a*), the deviation of the shape of the tube in the subsequent evolution from its initial shape increases as a result of the deformation by the three-dimensional convecting flow. In the case of an equipartition field ($B_0 = 1$; Fig. 6*a*), we find that the sections of the tube in the paths of the strong downdrafts are pushed downward and are "pinned down" to the bottom of the domain, while the portions of the tube in the broad upflow regions rise to the surface.

The different dynamic behavior of the tube shown in Figure 6 from the case with $B = 10$ to the case with $B = 1$ corresponds to a transition from a magnetic-buoyancy–dominated evolution to a convection-dominated evolution. This transition can be understood by comparing the magnitude of the magnetic buoyancy force with that of the hydrodynamic force from convection, which can be estimated from the aerodynamic drag exerted on the tube. For magnetic buoyancy to dominate, we need

$$\frac{B_0^2}{8\pi h_0} > C_d \frac{\rho_0 v_c^2}{\pi a} \ . \tag{20}$$

When estimating the magnitude of the magnetic buoyancy, we have considered only the first term on the right-hand side of equation (19) and have ignored the modification due to twist (the $\frac{1}{2}q^2a^2$ term in the parentheses), since the dominant contribution comes from the $B_0^2/8\pi h_0$ term. Equation (20) leads to

$$B_0 > \left(\frac{2C_d}{\pi}\frac{h_0}{a}\right)^{1/2} B_{\rm eq} \sim \left(\frac{h_0}{a}\right)^{1/2} B_{\rm eq} \sim \left(\frac{H_p}{a}\right)^{1/2} B_{\rm eq} \ . \tag{21}$$

Here we have used the approximation that $2C_d/\pi$ is of the order of 1. The above equation states that the field strength of the flux tube needs to be significantly superequipartition [by a factor greater than about $(H_p/a)^{1/2} \sim 3$] in order for the magnetic buoyancy to be able to counteract the hydrodynamic force from the convective downflows. This is in agreement with the results shown in Figure 6, in which we find that for the case with the critical field strength $B_0 = 3$, the portions of the tube in the strong downdrafts are just barely able to rise under the buoyancy force.

3.2. *Evolution of Tubes with an Equipartition Field*

In the case of tubes with an equipartition field $B_0 = 1$ (Fig. 6*a*), the magnetic buoyancy is weaker than the hydrodynamic force resulting from the convective downdrafts; hence, the evolution of the tube depends sensitively on the local condition of the convective flow. Figure 7*a* shows the buoyancy distribution in the vertical plane that contains the axis of the initial flux tube with $B_0 = 1$. It can be seen that the flux tube is nearly uniformly buoyant. Figure 7*b* shows the buoyancy distribution in the same vertical slice at a later time ($t = 1.01H_r/v_c$), and we see that despite being buoyant, the portions of the flux tube in the downdrafts are pushed downward to the bottom. (Note that some segments of the flux tube have moved out of the plane, resulting in the discontinuous appearance in the buoyancy distribution.) The pinned-down flux is then further distorted and transported laterally by the horizontal diverging flow at the bottom. This is evident in the top two panels of Figure 8, which show two snapshots of the *y*-*z* cross section (perpendicular to the initial tube axis) at the location $x = 2.61H_r$, where the tube is being pushed down by the downdraft. The middle two panels of Figure 8 show two snapshots of the *y*-*z* cross section of the tube at $x = 6.82H_r$, where the tube is in an upflow region. This portion of the tube is found to rise to the surface at a significantly faster speed (by about 50%) than the steady rise speed ($\approx 0.15v_c$) obtained from the reference two-dimensional simulation (Ref A in Table 1) of the same buoyant tube ascending through the domain in the absence of convection. Snapshots of another *y*-*z* cross section of the tube at $x = 6.13H_r$ are shown in the bottom two panels of Figure 8. At this location, the rise of the tube is also boosted by a local upflow. However, as the tube cross section approaches the surface, it encounters a downdraft that severely distorts the tube cross section (see the bottom panel of Fig. 8).

The last panel of Figure 6*a* shows that an Ω-shaped emerging tube has formed with its two ends pinned down by the convective downdrafts. The development of this Ω-tube is a result of the three-dimensional convection rather than a buoyancy instability or an artificial variation in the initial buoyancy distribution. The length scale or footpoint separation of the Ω-tube is determined by the separation of the major downdrafts, which in the case shown in Figure 6*a* is about $5H_r$, a value significantly smaller than the minimum wavelength ($\sim 10H_r$) necessary for the onset of the magnetic

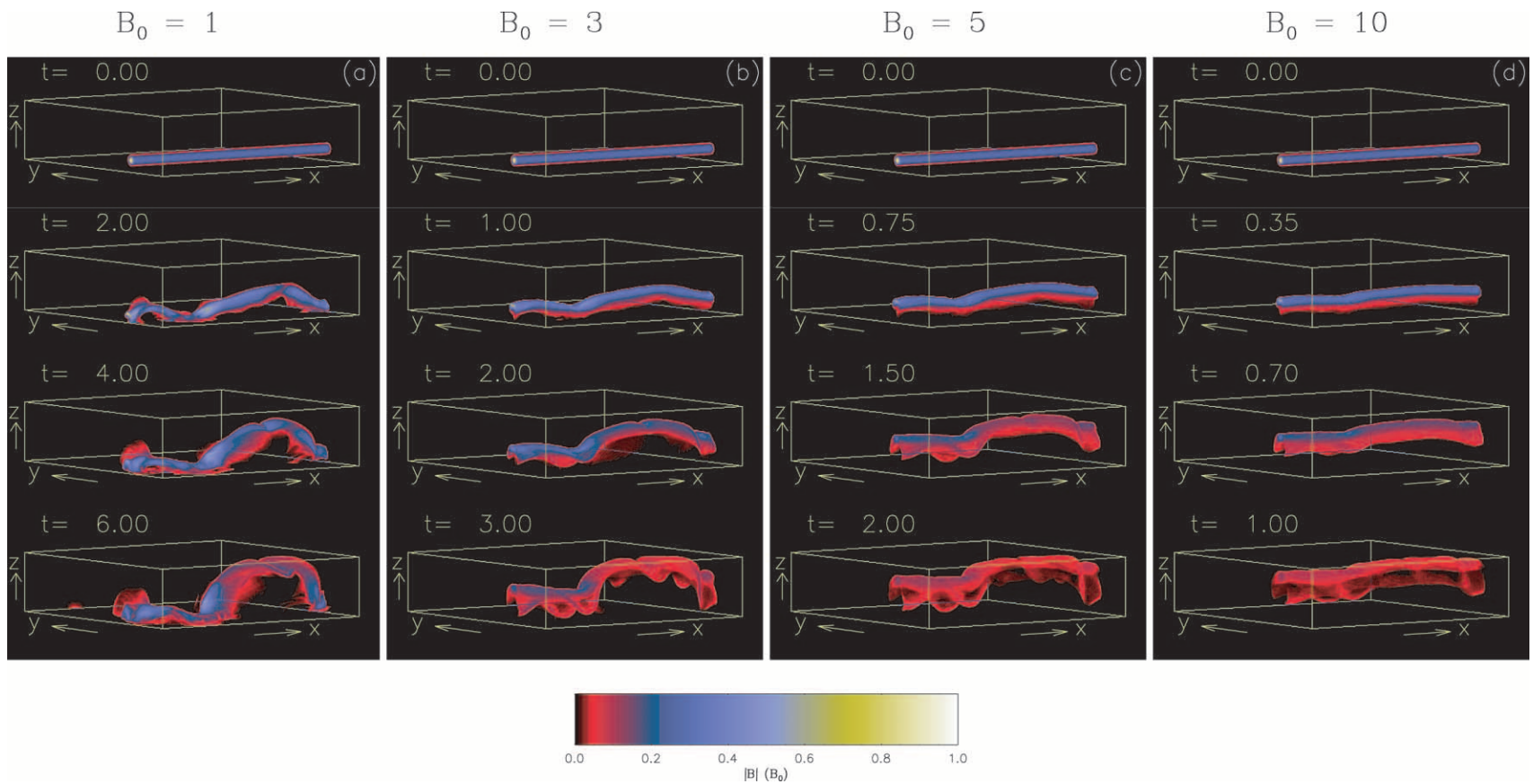

FIG. 6.—Evolution of the buoyant flux tube in the three-dimensional convective flow from runs (*a*) case A, (*b*) case B, (*c*) case C, and (*d*) case D. The values of B_0 are given in units of B_{eq}, and t is given in units of H_r/v_c. The images show the volume rendering of the absolute magnetic field strength of the flux tube.

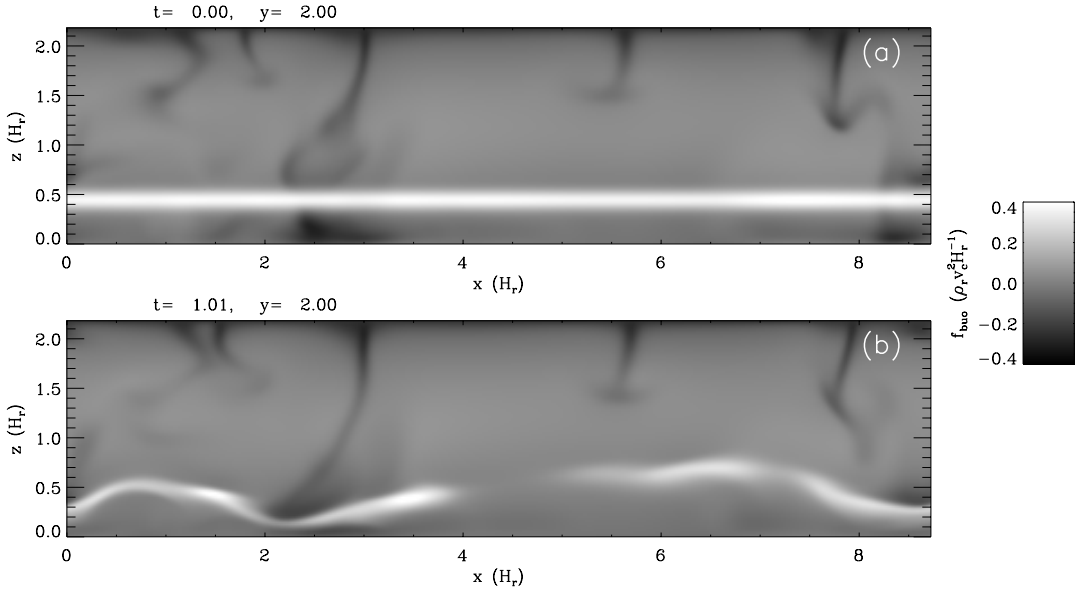

FIG. 7.—Distribution of buoyancy in the vertical plane that contains the axis of the initial flux tube at (*a*) $t = 0$ and (*b*) a later time $t = 1.01H_r/v_c$, for the case with $B_0 = 1$ (case A).

buoyancy instability for a toroidal field at the base of the solar convection zone. The Ω-tube is severely distorted by convection, as can be seen in Figure 9*a*, which shows two different views of the same tube shown in the bottom panel of Figure 6*a*. We see that the top of the Ω-tube meets another downdraft, which produces a local "indentation" of the tube (Fig. 9*a*, *top panel*). We cannot, however, rule out the above distorted rising Ω-tube (shown in Figs. 6*a* and 9*a*) as a possible progenitor of a solar active region, since the observed emerging magnetic regions often show complex morphologies that are not inconsistent with such a distorted emerging tube. Figure 10*a* shows the morphology of the vertical magnetic field (*contours*) in a horizontal cross section taken near the top of the Ω-tube (at $z = 1.86H_r$). It suggests that the initial emergence may produce two adjacent bipolar regions on the surface, each of which shows an apparent tilt of about 30° from the *x*-direction (east-west direction). The apparent tilts are caused by distortion of the tube by convection. To obtain a more statistically significant measure of the tilting or north-south bending of the flux tube caused by convection, we calculate an rms tilt of the entire tube as follows: We evaluate the field weighted-average *y*-position ($\overline{y}$) of the tube as a function of *x* along the tube and then calculate the rms of $\tan^{-1}(d\overline{y}/dx)$. This rms tilt for the tube is about 27°. The observed solar active region tilts have a large scatter about the mean tilt given by Joy's law, with the rms of the scatter ranging from about 10° to 30° depending on the size of the regions (Fisher et al. 1995). The scatter in active region tilts is most likely a result of convection acting on rising flux tubes (Fisher et al. 1995; Longcope & Fisher 1996). The tilting of the tube caused by convection obtained from our simulation in the case with $B_0 = 1$ is greater than the rms scatter of the tilts of large active regions (10°) but is not beyond the rms scatter of small active regions (30°).

Interestingly, we find that for buoyant tubes with $B_0 = 1$, the dynamic evolution is no longer sensitive to the initial twist of the tube, in contrast to what was found from the simulations in the absence of convection. Figure 9*b* shows the configuration of the tube at $t = 6H_r/v_c$ resulting from a run (case E) that is the same as that shown in Figure 9*a* except that the initial twist q is set to 0 instead of $q = 0.25a^{-1}$. Figure 10*b* shows B_z in the horizontal cross section near the top of the Ω-tube (at $z = 1.86H_r$) for the case with $q = 0$, in comparison with the case of $q = 0.25a^{-1}$ shown in Figure 10*a*. We see that the morphology of the tube in the case with no initial twist is nearly indistinguishable from that with $q = 0.25a^{-1}$. In the present case of convection-dominated evolution, the flux tube is being bent by the flow in an incoherent manner along the tube, and Ω-shaped tubes form between strong downdrafts. The flux tube is no longer able to develop vortex tubes coherent along the tube axis, as would be the case in the absence of convection. Because of the three-dimensional nature of the flux tube, the restoring tension force that acts against distortion by convection depends mainly on the *total* field strength of the tube rather than just the azimuthal field component. For $q = 0.25a^{-1}$, the peak azimuthal field strength in the initial tube cross section is only about $0.1B_0$, small compared to the peak axial field strength B_0. Hence, the total field strength for the twisted tube of $q = 0.25a^{-1}$ is not significantly different from the untwisted tube, which leads to the very similar three-dimensional evolution of the tubes in the convective flow.

3.3. *Evolution of Tubes with a Highly Superequipartition Field*

For buoyant tubes with a highly superequipartition field, magnetic buoyancy dominates the hydrodynamic force from convection, and the evolution of the tubes converges to the simulation result of the buoyant rise of the same horizontal flux tubes in a static, adiabatically stratified fluid. Figure 11 shows the rise velocity of the tube (with $B_0 = 10$, $q = 0.25a^{-1}$) measured in two different cross sections at $x = 2.34H_r$ and $6.63H_r$, which are respectively located in a strong downdraft and an upflow

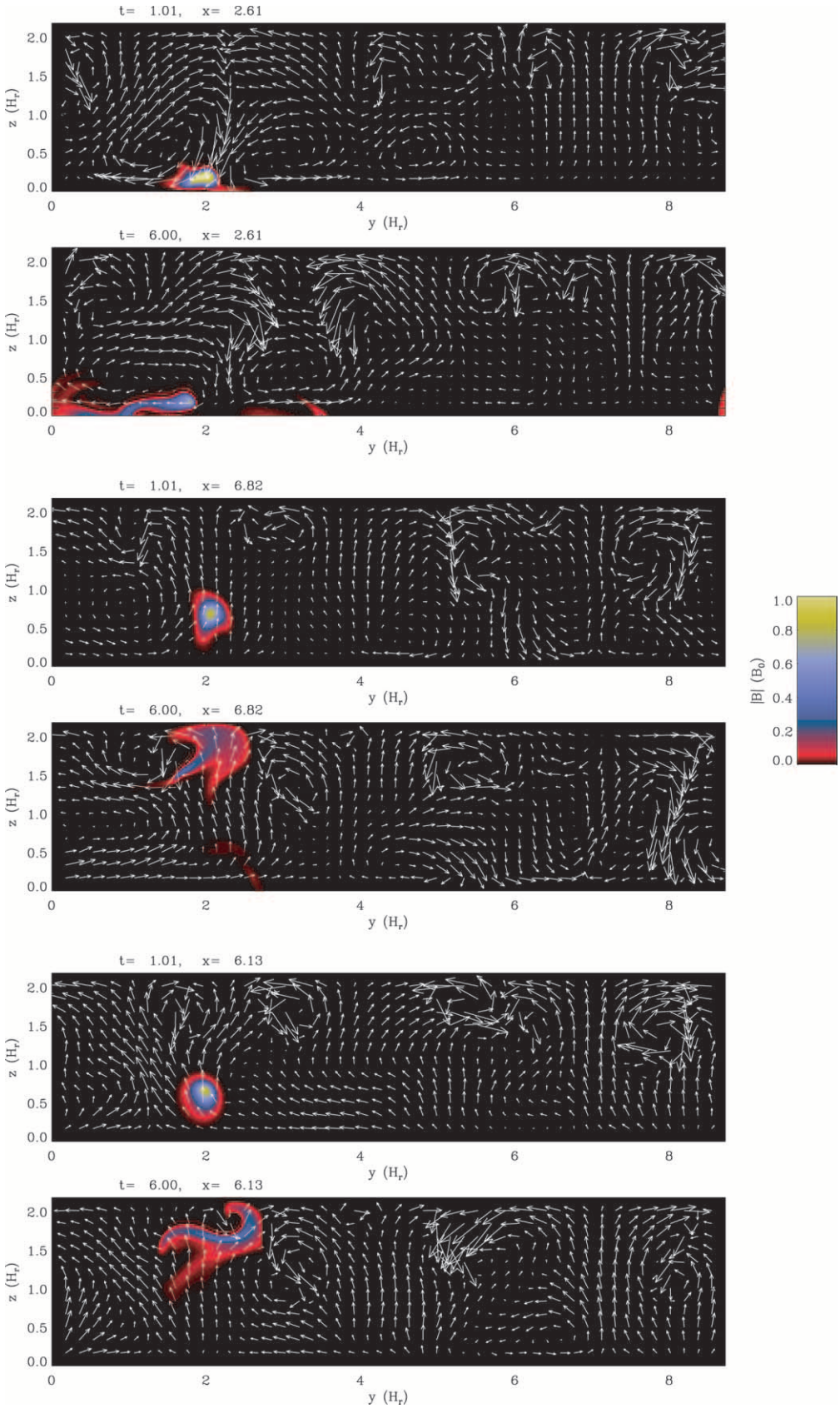

FIG. 8.—Snapshots of the velocity field and the absolute magnetic field strength in several different y-z cross sections (perpendicular to the initial tube axis) at different times during the evolution of the tube with $B_0 = 1$ (case A). The marked time t is given in units of H_r/v_c.

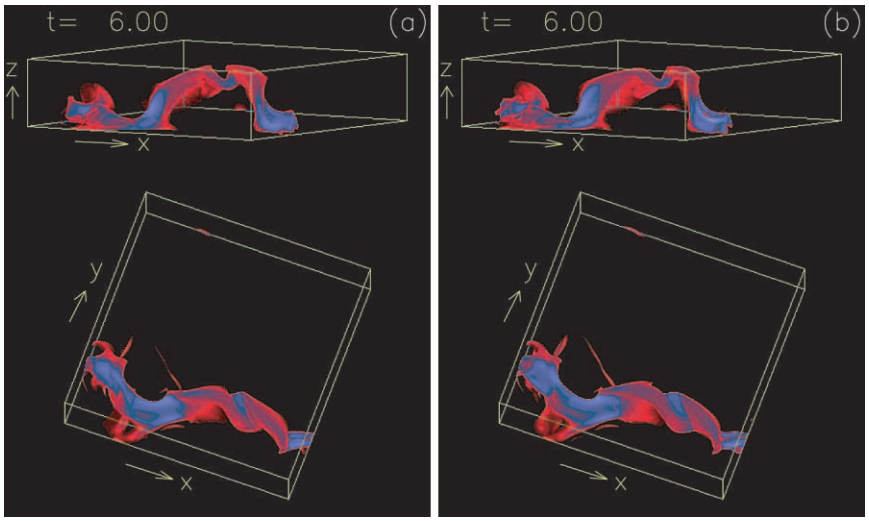

FIG. 9.—(*a*) Two different views of the same tube shown in the bottom panel of Fig. 6*a* resulting from the run of case A. (*b*) Same as (*a*), except for being from a run without an initial twist (case E).

region. The rise velocity is evaluated at the position of the peak field strength in the tube cross section. For comparison, the rise velocity obtained from the reference simulation (Ref D) of the same buoyant tube in the absence of convection is also shown. We can see that the tube rise velocities in the convecting flow (both in the downdraft location and in the upflow region) are similar to that of the reference simulation. Regardless of the different initial vertical velocities at different positions along the tube (e.g., $-0.71v_c$ in the downdraft location and $0.26v_c$ in the upflow location, as shown in Fig. 11), the tube accelerates under its buoyancy to a steady velocity of approximately $1.5v_c$. The bending of the tube resulting from distortion by the three-dimensional convective flow is small, and the tube essentially retains its initial straight horizontal configuration. The final shape of the tube is determined by the initial buoyancy distribution along the tube.

Figures 12*b* and 12*c* show cross sections of the rising tube at $x = 2.34H_r$ (in the path of a strong downdraft) and $6.63H_r$ (in an upflow region), compared with the tube cross section obtained from the reference run (Ref D) in the absence of convection (Fig. 12*a*). It can be seen that the tube cross sections are not significantly distorted by the presence of the convective flow. In the present case of magnetic-buoyancy–dominated evolution, we find that the cohesion of the tube still depends sensitively on the initial twist. Without twist, the buoyant tube breaks up into two long vortex tubes that move apart horizontally, as can be seen in Figure 13, which shows the evolution obtained from the run of case F (same as case D shown in Fig. 6*d*, except that the initial twist q is set to 0).

The earlier work of Dorch et al. (2001) also modeled the rise of a horizontal flux tube with a highly superequipartition field strength ($B = 10B_{\rm eq}$) in a stratified convecting model convection zone. However, they used a significantly

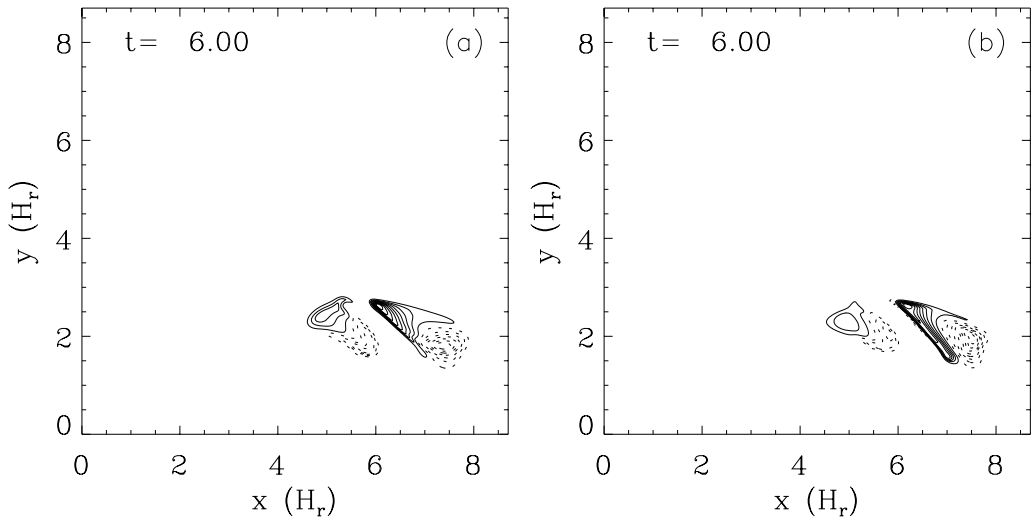

FIG. 10.—(*a*) Morphology of the vertical magnetic field B_z (*contours*) in a horizontal cross section taken near the top of the Ω-tube shown in Fig. 6*a* (from the run of case A) at the height $z = 1.86H_r$. Solid contours correspond to a positive vertical field, while dotted contours correspond to a negative vertical field. (*b*) Same as (*a*), except for being from a run without a twist (case E).

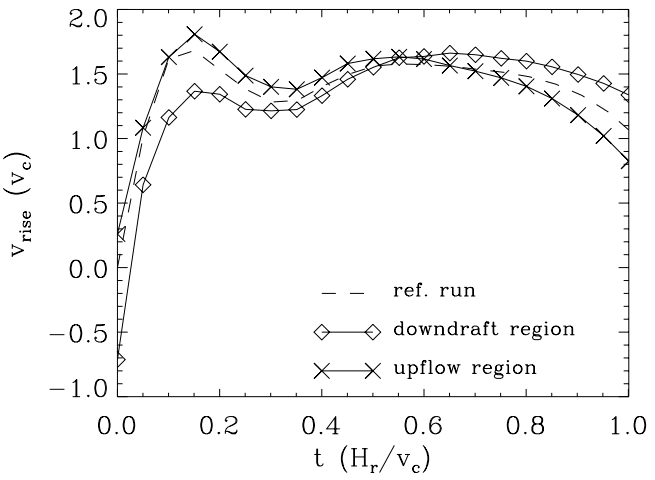

FIG. 11.—Rise velocity of the tube (with $B_0 = 10$, $q = 0.25a^{-1}$, case D) measured in two different tube cross sections at $x = 2.34H_r$ and $6.63H_r$, which are respectively located in a strong downdraft and an upflow region. Also shown for comparison is the rise velocity obtained from the reference simulation (Ref D) of the same buoyant tube in the absence of convection.

higher twist for the flux tube, with $q = a^{-1}$, which is at the marginal stability for the kink instability and is 4 times the highest twist we have considered here ($q = 0.25a^{-1}$). Their calculation is fully compressible with plasma $\beta \sim 100$, which may be more suitable for describing the dynamics of rising flux tubes in the upper layers of the convection zone. The results from our simulation with $B = 10B_{eq}$ (case D) are in qualitative agreement with theirs in that the tube remains straight and the rise speed, rise time, and the rise trajectory are not significantly altered by the presence of convection. In addition, Dorch et al. (2001) found significantly more flux loss for the rising flux tube in the presence of convection (about 20% of the initial flux is lost through the rise) in comparison to their reference two-dimensional run without convection (in which case the flux loss is negligible). In our case, we find that at a twist of $q = 0.25a^{-1}$, the flux tube already suffers a flux loss of about 30% to the wake during its rise in the *absence* of convection (see also Emonet & Moreno-Insertis 1998). However, we do not see as large an increase of flux loss due to the presence of convection as was found in Dorch et al. (2001). As can be seen in the comparison of tube cross section morphology shown in Figure 12, the distortion of the cross sections of the flux tube in the convective flow (Figs. 12*b* and 12*c*) is not substantially more severe in comparison to the two-dimensional reference case (Fig. 12*a*) at this high field strength. For the tube cross section shown in Figure 12*b* (in the path of a strong downdraft), about 38% of the total flux of the tube is pulled into the wake, while about 33% of the total flux is in the wake in the reference case without convection (Fig. 12*a*). For the cross section in the updraft region (Fig. 12*c*), the amount of flux in the wake is nearly the same as that for the reference case (Fig. 12*a*). It is not clear what causes this difference between our result and that of Dorch et al. (2001) with regard to the increase of flux loss due to convection for highly super-equipartition tubes. One possibility is the treatment of the viscosity. Our simulations use an explicit viscous term with constant ν, while Dorch et al. (2001) use a more sophisticated treatment in which fluid is much less diffusive in smooth regions than in regions where a steep gradient exists.

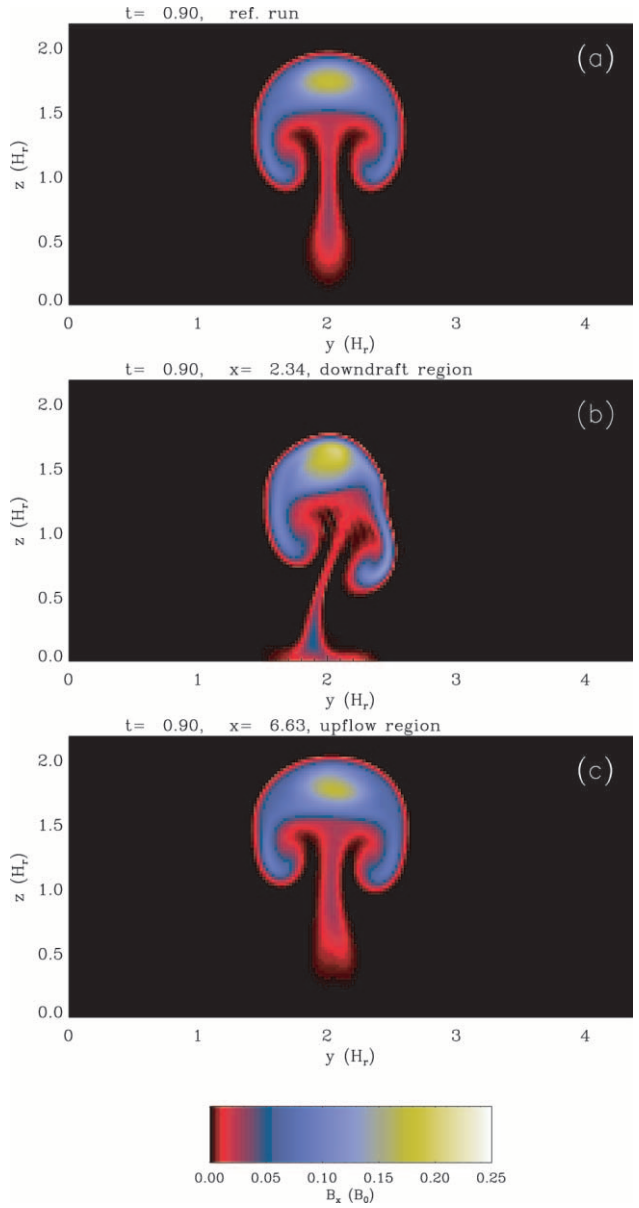

FIG. 12.—(*a*) Snapshot of the rising tube cross section from the two-dimensional reference simulation Ref D. Cross sections of the rising tube are shown at (*b*) $x = 2.34H_r$ (in the path of a strong downdraft) and (*c*) $6.63H_r$ (in an upflow region) from the run of case D with $B_0 = 10$ and $q = 0.25a^{-1}$. The marked time t is in units of H_r/v_c.

In our case, the effective Reynolds number for the rising flux tube is rather small: $\mathrm{Re}_{\mathrm{eff}} = v_{\mathrm{rise}}a/\nu \sim 40$. The sophisticated treatment of viscosity described in Dorch et al. (2001) allows for a more turbulent flow with more energy in the smaller scales. This may result in additional distortion of magnetic flux tubes not evident in our simulations.

4. DISCUSSION AND CONCLUSIONS

We have carried out direct numerical simulations of the dynamic evolution of buoyant magnetic flux tubes in three-dimensional stratified convection. To most clearly identify the effect of convection on the tube, we focus on the simple case in which the initial flux tubes are uniformly buoyant along their axes so that the development of three-

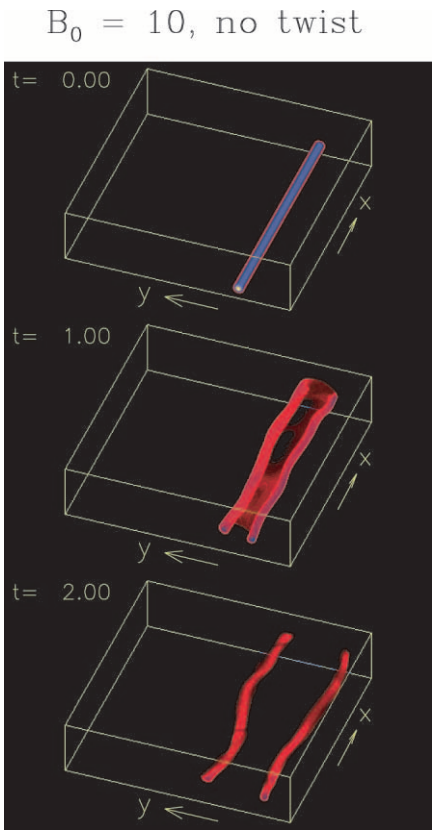

FIG. 13.—Evolution of the tube from the run of case F with $B_0 = 10$ and zero initial twist. The images show the volume rendering of the absolute field strength. See Fig. 6 for the color table. The time t is given in units of H_r/v_c.

dimensionality in the subsequent evolution is due to convection. We consider twisted flux tubes with initial axial field strengths B_0 ranging from B_{eq} to $10B_{eq}$ and twist q ranging from 0 to $0.25a^{-1}$, where B_{eq} is the field strength in equipartition with the kinetic energy of the strongest downdrafts and q denotes the angle of field line rotation about the axis over a unit length along the tube. Reference simulations of the same tubes in the absence of convection are also carried out for comparison.

We find that the evolution of the buoyant tubes changes from being "convection dominated" to "magnetic buoyancy dominated" as the field strength increases from B_{eq} to $10B_{eq}$. The field strength of the flux tube needs to be significantly superequipartition, $B_0 > (H_p/a)^{1/2}B_{eq}$, in order for the magnetic buoyancy of the tube to be able to overcome the hydrodynamic force from the convective downflows. Applying the appropriate values for H_p, a, and B_{eq} at the base of the solar convection zone, $H_p \sim 5.6 \times 10^9$ cm, $a \lesssim 5.6 \times 10^8$ cm, and $B_{eq} \sim 10^4$ G, the above criterion corresponds to $B_0 > 3 \times 10^4$ G.

For a tube of equipartition field strength ($B_0 = B_{eq}$), the evolution and morphology of the tube are largely controlled by the local conditions of the convective flow. Sections of the tube in the paths of strong downdrafts are pinned down to the base of the domain, while the rise speeds of sections within the upflow regions are significantly boosted; Ω-shaped emerging tubes can form between downdrafts. The footpoint separation of the Ω-tube is given by the separation of downdrafts and does not reflect the initial buoyancy distribution along the tube. Furthermore, we find that the three-dimensional evolution and structure of the flux tubes with $B_0 = B_{eq}$ no longer depend sensitively on the initial twist (compare Figs. 9*a* and 9*b*), in contrast to the results obtained in the absence of convection.

Although flux tubes with $B_0 = B_{eq}$ are found to be severely distorted by the convective flow, we cannot rule out the distorted Ω-tubes that emerge between downdrafts (see, e.g., Figs. 9 and 10) as a possible source of solar active regions, given the fact that the observed emerging magnetic regions often show complex morphologies. In our simulations with $B_0 = B_{eq}$, the random tilting of the flux tube caused by convection is of the amplitude of about 30°. This amplitude is greater than the rms scatter of the tilt angles of large active regions (10°) but is not beyond the rms scatter of the tilts of small active regions (30°). We note that the convective distortion of flux tubes in our simulations is likely an underestimate. The solar convection zone is significantly more stratified and the convective flow is certainly more turbulent than what we can model in our simulations. Taking this into consideration, tubes of an equipartition field may be too severely distorted by convective flows to be consistent with the observational constraint on the dispersion of active region tilt angles.

As the tube field strength B_0 increases above the critical value of $\sim(H_p/a)^{1/2}B_{eq}$, the dynamic evolution converges toward the results of previous simulations of the buoyant rise of magnetic flux tubes in a static, adiabatically stratified model solar convection zone (e.g., Emonet & Moreno-Insertis 1998; Fan et al. 1998). In the case of $B_0 = 10B_{eq}$, we find that the flux tube essentially retains its initial shape of a straight horizontal tube during its ascent. This is because the buoyancy distribution along the tube is uniform, and the hydrodynamic force from the convective flow is too weak to introduce any significant bending of the tube. The rise speed is not significantly altered by the presence of convection. The cohesion of the rising flux tube still depends sensitively on the initial twist of the tube, as was found in previous two-dimensional simulations in the absence of convection (Longcope et al. 1996; Emonet & Moreno-Insertis 1998; Fan et al. 1998).

In a subsequent paper, we will extend our investigation to model tubes with nonuniform initial buoyancy distribution along the axes and will study the buoyant rise of arched tubes in a three-dimensional convective flow. The effect of rotation will also be incorporated to study how the Coriolis force in conjunction with convection determines the tilt of the emerging Ω-loops.

We thank Peter Gilman for helpful comments on the manuscript. Part of this work was carried out while the authors were participants in the program on the solar magnetic field at the Institute for Theoretical Physics (ITP), University of California, Santa Barbara. We acknowledge support by NSF grant PHY 99-07949 awarded to the University of California, Santa Barbara during our participation in the solar program at ITP. G. H. F. and W. P. A. were also supported by grants from the NASA Sun-Earth Connection Supporting Research and Technology program, the NASA Astrophysics Theory program, and the NASA Sun-Earth Connection Theory program through a subcontract.

APPENDIX

A NOTE ON THE DIFFERENT DEFINITIONS OF THE REFERENCE ATMOSPHERE USED IN THE PRESENT PAPER AND LANTZ & FAN (1999)

In this appendix we clarify a difference in the definition of the reference atmosphere used in the present paper compared to that in Lantz & Fan (1999). In Lantz & Fan (1999), the reference atmosphere (denoted by T_0, p_0, ρ_0, and s_0) was defined to correspond strictly to the zero-order balance in the anelastic scaling, which is an adiabatically stratified equilibrium atmosphere, since to zero order, $ds_0/dz = 0$ or $s_0 = 0$ (or any constant; see eq. [38] in Lantz & Fan 1999). A separate *time-independent*, first-order $O(\delta)$ entropy gradient $ds_d(z)/dz$ called the "drive function" was then added (see eq. [55] and the text that follows and also eq. [72] in Lantz & Fan 1999) to make the atmosphere convectively unstable and initiate convection. The subsequent fluctuating part of the entropy due to the onset of convection is denoted by $\tilde{s}_1$, and the sum of the time-independent $s_d(z)$ and the fluctuating $\tilde{s}_1$ is denoted by s_1 in that paper. Lantz & Fan (1999) used the above notations to emphasize that the imposed $s_d(z)$ and the subsequent fluctuating $\tilde{s}_1$ are both first-order $O(\delta)$ quantities. Here we have chosen to use the more "conventional" definitions (following Glatzmaier 1984), where the time-independent reference state (denoted by T_0, p_0, ρ_0, and s_0) is defined to be a *weakly* superadiabatically stratified equilibrium atmosphere with an $O(\delta)$ entropy gradient $ds_0(z)/dz$. Therefore, the reference atmosphere (T_0, p_0, ρ_0, s_0) does not correspond strictly to the zero-order balance, and we have attributed the $O(\delta)$ entropy gradient $ds_d(z)/dz$ in Lantz & Fan (1999) to $ds_0(z)/dz$. The reference atmosphere here is defined to correspond to the equilibrium state before the onset of large-scale convective motions. The subsequent fluctuating part of the entropy is denoted by s_1, and as we have noted in our paper, both $s_0(z)$ and s_1 are $O(\delta)$ quantities. The difference described above between our present paper and Lantz & Fan (1999) is merely in the notation. Introducing a separate $ds_d(z)/dz$ to the zero-order isentropic atmosphere as is done in Lantz & Fan (1999) is effectively the same as using a reference atmosphere that is weakly superadiabatically stratified, as we have done here. The basic assumption used in both papers is the same: under the anelastic approximation, the entropy gradient is 0 to zero order, and its leading (lowest) order term is $O(\delta)$, or in other words, the entropy gradient remains much smaller than c_p/H_p.

REFERENCES

Abbett, W. P., Fisher, G. H., & Fan, Y. 2000, ApJ, 540, 548
———. 2001, ApJ, 546, 1194
Chandrasekhar, S. 1961, Hydrodynamic and Hydromagnetic Stability (New York: Dover)
Dorch, S. B. F., Gudisken, B. V., Abbett, W. P., & Nordlund, Å. 2001, A&A, 380, 734
Dorch, S. B. F., & Nordlund, Å. 1998, A&A, 338, 329
Emonet, T., & Moreno-Insertis, F. 1998, ApJ, 492, 804
Fan, Y. 2001, ApJ, 546, 509
Fan, Y., Zweibel, E. G., & Lantz, S. R. 1998, ApJ, 493, 480
Fan, Y., Zweibel, E. G., Linton, M. G., & Fisher, G. H. 1999, ApJ, 521, 460
Fisher, G. H., Fan, Y., & Howard, R. F. 1995, ApJ, 438, 463
Fisher, G. H., Fan, Y., Longcope, D. W., Linton, M. G., & Pevtsov, A. A. 2000, Sol. Phys., 192, 119
Gilman, P. A., & Glatzmaier, G. A. 1981, ApJS, 45, 335
Glatzmaier, G. A. 1984, J. Comput. Phys., 55, 461
Hale, G. E., Ellerman, F., Nicholson, S. B., & Joy, A. H. 1919, ApJ, 49, 153
Howard, R. F. 1991, Sol. Phys., 136, 251
Lantz, S. R., & Fan, Y. 1999, ApJS, 121, 247
Longcope, D. W., & Fisher, G. H. 1996, ApJ, 458, 380
Longcope, D. W., Fisher, G. H., & Arendt, S. 1996, ApJ, 464, 999
Moreno-Insertis, F. 1997, Mem. Soc. Astron. Italiana, 68, 429
Rayleigh, J. W. Strutt, Lord 1916, Philos. Mag., 32, 529
Spruit, H. C. 1981, A&A, 98, 155
Spruit, H. C., & van Ballegooijen, A. A. 1982, A&A, 106, 58
Stein, R. F., & Nordlund, Å. 1989, ApJ, 342, L95
———. 2000, Sol. Phys., 192, 91
Wissink, J. G., Matthews, P. C., Hughes, D. W., & Proctor, M. R. E. 2000, ApJ, 536, 982